# Novel characterization of the adsorption sites in large pore metal–organic frameworks: combination of X-ray powder diffraction and thermal desorption spectroscopy

**Ali Soleimani-Dorcheh,[ab] Robert E. Dinnebier,[c] Agnieszka Kuc,[d] Oxana Magdysyuk,[c] Frank Adams,[c] Dmytro Denysenko,[e] Thomas Heine,[d] Dirk Volkmer,[e] Wolfgang Donner[b] and Michael Hirscher*[a]**

The preferred adsorption sites of xenon in the recently synthesized metal–organic framework MFU-4*l*(arge) possessing a bimodal pore structure (with pore sizes of 12 Å and 18.6 Å) were studied *via* the combination of low temperature thermal desorption spectroscopy and *in situ* X-ray powder diffraction. The diffraction patterns were collected at 110 K and 150 K according to the temperature of the desorption maxima. The maximum entropy method was used to reconstruct the electron density distribution of the structure and to localize the adsorbed xenon using refined data of the Xe-filled and empty sample. First principles calculations revealed that Xe atoms exclusively occupy the Wyckoff 32f position at approximately 2/3 2/3 2/3 along the body diagonal of the cubic crystal structure. At 110 K, Xe atoms occupy all 32 f positions (8 atoms per pore) while at 150 K the occupancy descends to 25% (2 atoms per pore). No Xe occupation of the small pores is observed by neither experimental measurements nor theoretical studies.

## 1. Introduction

The term Metal–Organic Framework (MOF) is generally referred to as a new class of hybrid coordination polymers consisting of metal oxide nodes or clusters that are connected by organic linkers and form highly porous frameworks. This class of microporous materials provides large specific surface area (SSA), high porosity and low mass density. The structure and properties of MOFs can be manipulated in different ways, such as using different linkers or metal sources, functionalizing the internal surface or doping guest molecules in the porous structure. Owing to their tuneable structure and unique physico-chemical properties, they are attracting a tremendous amount of interest in different areas such as gas storage, gas separation, catalysis and biomedical applications. Among them, gas storage and separation is of the greatest interest.[1–5]

In order to enhance the storage capacity or selectivity of a MOF, it is very important to identify the adsorption sites in the porous structure and to tune them to optimize storage of a guest molecule of certain size. Detailed identification of adsorption sites in MOFs containing large pores remains a challenge. Several methods are commonly employed for this purpose, among which molecular simulation is the most-widely used one.[6–8] However, besides the computational study, accurate experimental methods are necessary to confirm the predictions provided by simulation. Neutron diffraction, inelastic neutron scattering and inelastic neutron spectroscopy have already been used for investigating deuterium and deutero-methane adsorption sites in MOFs.[9–12] However, these methods require either a neutron reactor or a spallation source. Alternatively, thermal desorption spectroscopy (TDS) is a powerful technique for investigating adsorption sites with different adsorption strength in MOFs. However, this method does not provide atomistic structural information about the adsorption sites.[13]

In order to have a comprehensive overview about the position and strength of the adsorption sites, a combination of methods with ease of access is demanded. In this article, we report about our study of Xe adsorption sites in a recently synthesized MOF, MFU-4*l*, using low-temperature TDS,

[a] *Max Planck Institute for Intelligent Systems, Heisenbergstr. 3, 70569 Stuttgart, Germany. E-mail: hirscher@is.mpg.de, soleimani@dechema.de; Fax: +49 711 689 1952; Tel: +49 711 689 1808*
[b] *Department of Materials Science, Darmstadt University of Technology, 64287 Darmstadt, Germany. E-mail: wdonner@tu-darmstadt.de; Fax: +49 6151 16 6023; Tel: +49 6151 16 6412*
[c] *Max Planck Institute for Solid State Research, Heisenbergstr. 1, 70569 Stuttgart, Germany. E-mail: r.dinnebier@fkf.mpg.de; Fax: +49 711 689 1139; Tel: +49 711 689 1503*
[d] *School of Engineering and Science, Jacobs University Bremen, 28759 Bremen, Germany. E-mail: t.heine@jacobs-university.de; Fax: +49 421 200 49 3223; Tel: +49 421 200 3223*
[e] *Institute of Physics, Augsburg University, 86135 Augsburg, Germany. E-mail: dirk.volkmer@physik.uni-augsburg.de; Fax: +49 (0)821 598 5955; Tel: +49 (0)821 598 3006*

*in situ* X-ray powder diffraction, and by means of first principles calculations of the interaction between Xe atoms and the nanoporous MFU-4*l* lattice.

## 2. Methods

MFU-4*l* has been synthesized by a solvothermal method using $ZnCl_2$ and $H_2$-BTDD (bis(1*H*-1,2,3-triazolo[4,5-*b*],[4′,5′-*i*])-dibenzo[1,4]dioxin) in *N*,*N*-dimethylformamide as a solvent. The detailed procedure can be found in ref. 14.

### 2.1 Thermal desorption spectroscopy (TDS)

The low temperature TDS has been conducted *via* an in-house designed apparatus formerly used for $H_2/D_2$ desorption studies. The setup was modified in order to measure the desorption spectrum of the physisorbed xenon. The apparatus and the measurement procedure are well explained in ref. 13–15. The amount of sample was always kept low (2–5 mg) to avoid readsorption during the measurements. Before starting the measurements, the sample was outgassed over night at 423 K under high vacuum conditions. Xenon (99.9(4)% (Westfalen AG)) was introduced by filling the chamber at a constant pressure. All measurements were conducted under the same experimental conditions such as loading time, cooling time, vacuum range, and heating rate. The spectra were recorded in the temperature range from 77–250 K. Besides $m/z = 129$ representing xenon, other signals such as $m/z = 18$ and 28 corresponding to water and nitrogen were monitored during the measurements.

### 2.2 *In situ* X-ray powder diffraction

High resolution X-ray powder diffraction (HRPD) patterns of MFU-4*l* loaded with Xe were collected at low temperatures on a laboratory powder diffractometer (D8, Bruker, Cu$K\alpha_1$ radiation from a primary Ge(111)-Johannson-type monochromator; a Våntag-1 position sensitive detector (PSD) with an opening angle of 6°) in Debye–Scherrer geometry with the sample in an open quartz glass capillary of 0.5 mm diameter (Hilgenberg). For gas loading, a modified version of an *in situ* capillary cell (Brunelli and Fitch, 2003) was used which allows 180° rocking of the capillary. In order to be able to switch between vacuum pumping and gas loading, a T-connector to a turbo pump and a Xe gas bottle equipped with a needle valve was attached. For heating of the capillary, a water-cooled capillary heater on a slider (MRI-GmbH), while for cooling a Cryostream 600 cold air blower (Oxford Cryosystems), was attached in a horizontal system.

The experimental conditions (temperature and loading pressure) were selected according to one of the desorption spectra.

The sample was outgassed under vacuum at 423 K for 6 hours before and one hour after loading the capillary. Xenon was loaded at 20 mbar and room temperature. Prior to the first measurement the capillary was cooled down to 110 K. Afterwards, the capillary was heated to 150 K under vacuum conditions. Once the temperature stabilized, a second powder pattern was measured. The sample was rocked during measurement for better particle statistics. Data were taken in steps of 0.017° $2\Theta$ with a total scanning time of 11 h.

### 2.3 Crystallographic localization of xenon atoms

For structure determination and refinement, the software TOPAS 4.2[16] was used. Starting coordinates for the framework structure of -4*l* were taken from the CCDC database (#776578).[17] Additional peaks could be assigned to crystalline ice-1h and solid xenon.

The peak profile and precise lattice parameters were determined by Le Bail fits[18] using the Fundamental Parameter (FP) approach of TOPAS.[19] Due to the fact that the geometry of the Våntac-1 PSD is not fully characterized by FP's, fine tuning of the available parameters was performed by using refined values of the FP's from a precise measurement of the NIST line profile standard SRM 660a (LaB6) in a 0.1 mm capillary over the full two theta range of the diffractometer.[20] For the modeling of the background, Chebyshev polynomials were employed. In addition, the amorphous hump originating from the quartz capillary was successfully modeled by a broad Lorentzian-shaped peak. The refinement converged quickly.

The crystal structure of the Xe loaded MFU-4*l* was solved by the global optimization method of Simulated Annealing (SA) in real space as implemented in TOPAS.[21] In the beginning, several Xe atoms were introduced into the SA process using a merging radius of 0.6, as proposed by Favre-Nicolin and Cerny.[22] To allow for additional flexibility in the structure determination process, the occupancies of all Xe atoms were introduced as additional variables. Within seconds, a unique crystallographic position occupied by Xe atoms was found, with different fractional occupancies and displacement factors in dependence on temperature.

The Maximum Entropy Method (MEM)[23,24] was used for finding eventually missing Xe atoms and for reconstruction of the electron density distribution of all Xe atoms in the unit cell. The prior information was provided by the electron density distribution corresponding to a refined independent spherical atom model (ISAM) using the same experimental data (procrystal density). In this model, the electron density is given as superposition of electron densities of free, non-interacting atoms placed at their refined positions and convoluted with refined thermal motion. All MEM calculations were performed using the program BayMEM,[25] employing the Sakata–Sato algorithm.[26]

The localization of the missing Xe atoms in the MOF was performed using experimental data sets – based on $F_{obs} + G$ (observed structure factors extracted after Rietveld refinements of empty/filled MOF with *G*-constraints for overlapping reflections). Observed structure factors extracted after Rietveld refinements of the empty MOF were used to find highly occupied positions of Xe atoms, while the data from the filled MOF allowed the detection of possibly additional low occupied positions and to reveal finer details on the distribution of electron density of the loaded gas.

As a result, initial data used for the MEM calculations did not contain any information about intercalated Xe atoms. The procrystal electron density was created from the Rietveld refinement of the incomplete structure (empty MOF). The analysis of the MEM reconstructed electron density was performed using the program EDMA.[25] This program allows determining not only the value of the electron density but also the integrated charge of atoms based on the Bader theory.

### 2.4 First principles simulations

The crystal structure of MFU-4*l* was fully optimized within Density-Functional Theory (DFT). We employed two different simulation models, a periodic and a cluster approach, thus having the possibility to compare strongly different setups. We selected the CRYSTAL09 code,[27] which makes use of periodic boundary conditions with explicit sampling of 29 distinct ***k*** points in the irreducible Brillouin zone, PBE exchange–correlation functional[28] and Gaussian-type basis functions, *i.e.* Cl_86-311G_apra_1993, Zn_86-411d31G_jaffe_1993, H_5-11G*_dovesi_1984, N_6-21G*_dovesi_1990, C_6-21G*_catti_1993, O_8-411_towler_1994. For the cluster model simulations, we treated finite cluster models using the ADF code[29] that employs Slater-type all-electron basis functions (DZP for C, H, O, N, Xe and TZP for Zn). In ADF, we modeled the fully saturated pore of MFU-4*l* (at the cut edges carbon atoms of the linkers are saturated with hydrogen atoms), leading to very similar structural properties (*i.e.* the Zn–Zn distance changes from 15.5 Å for the periodic structure to 15.7 Å for the cluster model). As Xe adsorption is dominantly a London dispersion interaction, besides the PBE we used the PBE-D and, for comparison, B88LYP-D exchange–correlation functionals that have been developed for such type of interactions.[30] Whenever possible, we exploited the point group symmetry to reduce computer cost.

## 3. Results

### 3.1. Thermal desorption spectroscopy

Fig. 1a shows the desorption spectra of Xe in MFU-4*l* initially loaded at pressures between 1 and 100 mbar. The desorption spectrum at $P = 1$ mbar is concentrated on a broad peak near 163 K. For $P = 20$ mbar, in addition to the high and broad maximum at 150 K, two additional peaks appear near 130 K and 190 K. Increasing the loading pressure to 50 mbar results in the same desorption profile as for $P = 20$ mbar with an additional peak centered near 170 K and several maxima at temperatures lower than 130 K. A further increase in the loading pressure to $P = 100$ mbar shows a similar profile of the spectrum as for $P = 50$ mbar at temperatures higher than 130 K, indicating the saturation of the material. Considering the boiling temperature of Xe, the peaks and shoulders at 130 K and below can be correlated to non-adsorbed gas atoms which are condensed on inter particle voids. These maxima are not observed for low coverage ($P = 1$ mbar), since all gas atoms are adsorbed and no excess gas exists. At 190 K, additionally a water desorption peak is observed which will affect the Xe desorption profile.

The stepwise desorption spectrum of MFU-4*l* loaded at 50 mbar Xe pressure is shown in Fig. 1b (heating rate $\beta = 0.1$ K s$^{-1}$). The first step, carried out between 90 K and 154 K, shows several maxima at temperatures below 130 K and one maximum at 152 K. Following an immediate cooling to 90 K, the second step was started from 90 K to 250 K. The second desorption curve shows a broad peak with lower intensity centered near 160 K. Since during the first step the condensed Xe has been desorbed, no significant desorption is detected below 130 K in the second run.

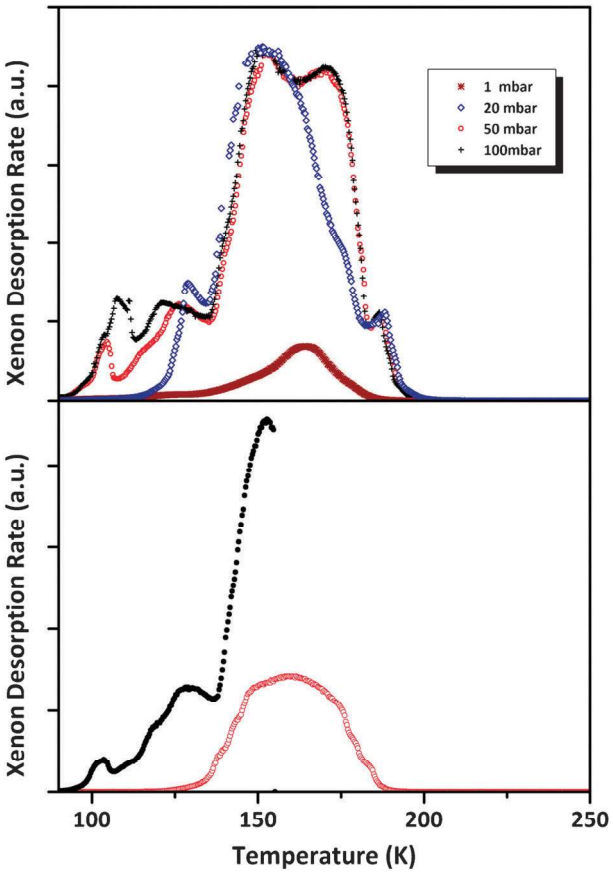


**Fig. 1** (a) Thermal desorption spectra of Xe in MFU-4*l* at different coverage for different loading pressures given in mbar. (b) Stepwise desorption spectra of Xe ($P = 50$ mbar). (●) shows the first and (○) shows the second measurement run.

### 3.2. *In situ* X-ray powder diffraction

According to the desorption spectrum for $P = 20$ mbar, PXRD measurements were performed at 110 K, where no desorption occurs, and 150 K, where the desorption rate is maximum. The refined diffraction pattern (Rietveld plot) of MFU-4*l* loaded with Xe at 20 mbar at 110 K is shown in Fig. 2.

The framework of MFU-4*l* contains two types of cavities alternating in three dimensions, which differ by the orientation of neighbouring chlorine atoms pointing towards or away from each other, thus leading to a bimodal pore structure. There are eight pores, four of each kind in the crystallographic unit cell. Both at temperatures of 110 K and 150 K, Rietveld and MEM analyses clearly reveal that the Xe atoms exclusively occupy the Wyckoff 32f position at approximately 2/3 2/3 2/3 along the body diagonal of the cubic crystal structure, relatively close to the pore walls. This means that due to space requirements, the Xe atoms exclusively occupy the four large pores of the unit cell, where the chlorine atoms are pointing away from each other. There are eight Xe atoms per pore forming a cube of edge length 10.183 Å. The nearest neighbours of the Xe atoms are nitrogen atoms at distances of 3.844 and 3.948 Å.

At $T = 110$ K, the 32f position is fully occupied, while at $T = 150$ K, the fractional site occupancy lowers to 25% in a

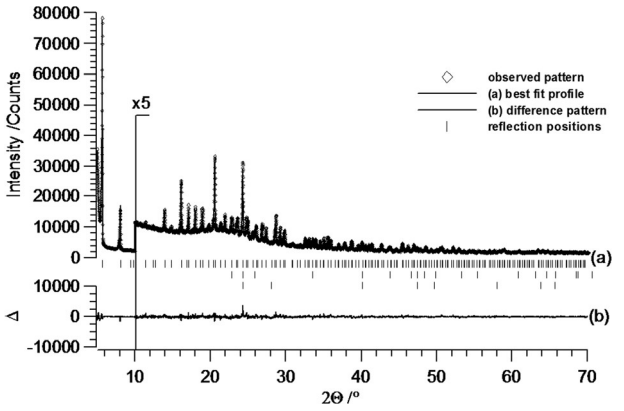


**Fig. 2** Scattered X-ray intensity for MFU-4*l* MOF loaded with Xe at $T$ = 110 K as a function of diffraction angle $2\Theta$. Shown are the observed pattern (diamonds), the best Rietveld-fit profile (line a), the difference curve between observed and calculated profiles (line b), and the reflection markers (vertical bars). The lower rows of reflection markers correspond to impurity phases, ice-Ih (middle row) and solid Xe (lower row). The wavelength was $\lambda$ = 1.54059 Å. The higher angle part of the plot starting at 10° $2\Theta$ is enlarged for clarity.

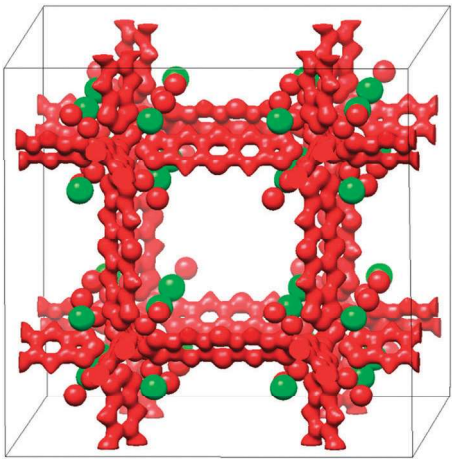

**Fig. 3** Three-dimensional MEM electron-density maps (MFU-4*l* structure (red) and adsorbed xenon atoms (green)) based on $F_{obs}$ + $G$. Contour levels: from 1 e Å$^{-3}$ for Xe filled MFU-4*l*.

statistical manner, which is calculated to be 2 instead of 8 Xe atoms per pore.

Fig. 3 shows the MEM reconstructed electron density of the data set taken at 110 K (created using the program UCSF Chimera) confirming the position of the Xe atoms from Rietveld refinement of the Xe filled and empty structures. It does not indicate any further atomic positions for Xe atoms. The distribution of the electron density of the Xe atoms was found to be fully isotropic ruling out certain types of positional disorder.

### 3.3. First principles simulations

In order to investigate the possibility of adsorption in small cavities, DFT calculations of the adsorption interaction in small and large cavities have been performed. The optimized fcc crystal structure of MFU-4*l* corresponds to unit cell parameters $a = b = c$ = 31.43 Å, in very good agreement

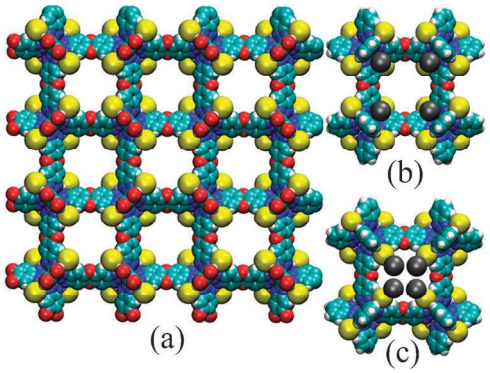


**Fig. 4** Bulk (a) and finite pore model structures with 4 Xe atoms in the large (b) and small (c) pore of MFU-4*l*. The atoms are shown in the van der Waals representation. Red – oxygen, dark blue – nitrogen, light blue – carbon, yellow – chlorine, gray – xenon, white – hydrogen, silver – zinc.

with the experimental value of 31.06 Å. As the error in the lattice parameters is only 1.2% (for comparison between experimental structure and both crystal and finite pore models), we can safely adopt the cluster model for the adsorption calculations. The bulk and finite pore structures of MFU-4*l* with four adsorbed Xe atoms are shown in Fig. 4. In the finite model we keep the full linkers surrounding the connector parts to account for the same environment of the adsorption sites as in the crystal structure. Adsorption energies with respect to the free gas phase Xe atoms are ~45 kJ mol$^{-1}$ for the large and ~5 kJ mol$^{-1}$ for the small pore, respectively. Details are given in Table 1.

## 4. Discussion

After adsorption of gases on a microporous material at low temperature, the desorption temperature is typically related to the strength of the adsorption sites. In the case of loading at low pressures (low coverage), the gas molecules occupy the sites with stronger interaction appearing at elevated temperature in the desorption spectrum. Upon increasing the coverage, weaker adsorption sites will be occupied appearing at lower temperature.[15] Additionally, if condensation of the gas occurs or impurity gases are adsorbed, extra desorption maxima may appear.

In the desorption spectrum (Fig. 1a), additional desorption peaks below 130 K and at 190 K appear for higher loadings which can be attributed to the solidification or liquefaction of the excess gas molecules and to the water desorption signal, respectively. The desorption maxima between 130 K and 190 K are attributed to the adsorption of Xe in the porous structure.

At the lowest loading pressure ($P$ = 1 mbar) the only desorption maximum appears at near 160 K. No condensation signal is observed at temperatures below 130 K, indicating that all Xe atoms are adsorbed on the porous structure. In the stepwise measurement, both spectra show the same desorption maximum near 160 K, which is related to an adsorption site in the porous structure.

As Fig. 1a shows that upon loading with higher pressure the structure gets saturated with Xe and a double peak structure

**Table 1** Calculated binding energies per Xe atom (in kJ $mol^{-1}$) and selected atomic distances (in Å) of MFU-4*l*

| System | PBE | | | PBE-D | | | BLYP-D | | | Experimental | |
|---|---|---|---|---|---|---|---|---|---|---|---|
| *Large pore* | | | | | | | | | | | |
| MFU-4*l* | $E_{bind}$ | Xe–Zn | Xe–N | $E_{bind}$ | Xe–Zn | Xe–N | $E_{bind}$ | Xe–Zn | Xe–N | Xe–Zn | Xe–N |
| 4Xe | 20.9 | 4.740 | 3.902 | 45.8 | 4.515 | 3.710 | 49.2 | 4.410 | 3.618 | 4.69 | 3.84 |
| *Small pore* | | | | | | | | | | | |
| MFU-4*l* | $E_{bind}$ | Xe–Cl | Xe–N | $E_{bind}$ | Xe–Cl | Xe–N | $E_{bind}$ | Xe–Cl | Xe–N | Xe–Cl | Xe–N |
| 4Xe | 0.99 | 4.179 | 8.99 | 5.1 | 3.904 | 8.639 | 4.8 | 4.141 | 8.993 | — | — |

[a] The linker sites are occupied but the adsorption energy decreases. This clearly indicates that MFU-4*l* has only one type of adsorption sites towards Xe.

appears at 150 K and 170 K, respectively. Usually, two desorption maxima indicate the existence of two adsorption sites. However, in the case of multiple adsorption sites, the stronger site should be occupied first, especially in large pore structures where the accessibility of gas molecules is better. Thus, the desorption maximum appearing at 170 K does not indicate a new adsorption site. Since it only appears at higher loadings, the signal may be related to the hindered diffusion of the gas in the more populated pores. Hence, in contrast to hydrogen which possesses two adsorption sites in MFU-4*l* in both cavities,[14] MFU4*l* hosts Xe only one adsorption site.

The PXRD pattern of the Xe filled MFU-4*l* at 20 mbar and 110 K shown in Fig. 2 confirms the observed solid Xe, as some of the gas remaining on the external surface has been solidified at 110 K. This is consistent with the desorption profile (Fig. 1a), that shows desorption maxima below 130 K.

While at $T = 110$ K, the 32f xenon site is fully occupied, at $T = 150$ K, the fractional site occupancy lowers to 25% in a statistical manner. This confirms that no other adsorption site is expected for Xe and the desorption maxima at high loading pressure appeared at 170 K (in Fig. 1a) and could be related to different configuration of the Xe atoms in adsorption sites and their population in large cavities during desorption.

The list of calculated and experimental interatomic distances between adsorbed Xe and its closest neighbours as well as the calculated adsorption energies for the interaction between the MFU-4*l* pores and the Xe atoms in both cavities are given in Table 1. The calculations indicate that in large pores the interaction is dominated by London dispersion interactions, as the dispersion-corrected functionals in agreement account for the largest portion of the adsorption energy. The two London-dispersion corrected functionals, with rather different exchange–correlation treatment, give very similar results for the adsorption energy and the geometry of the adsorbed noble gas atoms, which is 45.8 (49.2) kJ $mol^{-1}$ for Xe in the large pore. The Xe atoms are adsorbed in the corners of the cavity, close to the N and Zn atoms (Fig. 4). This explains and nicely agrees with the experimental thermal desorption spectra, where only one peak is observed for very low loadings of Xe. Those interactions are considerably stronger than those of $H_2$ or He, due to the larger polarizability of the noble gas atoms. Owing to the relatively large interaction energy and masses of the adsorbed atoms we expect that zero point energy corrections have a minor effect on the results. For comparison, Ryan *et al.*[31] have investigated the Xe interaction with HKUST-1 using a Grand Canonical Monte Carlo (GCMC) method and obtained heats of adsorption of 32 kJ $mol^{-1}$ for Xe.

For the small pores, we conclude that the binding energy is negligible (Table 1). For comparison, if one takes out the 4 Xe atoms as optimized from the small pore and calculates the binding energy of the cluster (with respect to individual Xe atoms) one obtains values of 0.4, 1.8 and 1.6 kJ $mol^{-1}$ per Xe atom at the PBE, PBE-D and BLYP-D levels, respectively, which is in the same order as the adsorption energy in the small pore of MFU-4*l* (Table 1). The free cluster of 4 Xe atoms with optimized bond distances has an even stronger binding energy (PBE-D level gives 2.0 kJ $mol^{-1}$).

Introducing more Xe atoms into the large pore in the form of a Xe cluster does not increase the adsorption energy. This indicates that there is no stabilization due to the formation of a Xe phase in the pores, which is in agreement with the experiment, where no clustering of Xe was observed.

In summary, our first-principles calculations support the experimentally observed adsorption sites of MFU-4*l* towards Xe atoms, which are situated in the corners of the larger pores, close to the Zn and N atoms. When more xenon is loaded to the pore, the linker sites are occupied but the adsorption energy decreases. This clearly indicates that MFU-4*l* has only one type of adsorption sites towards Xe.

## 5. Conclusion

A new combination of characterization methods is used to identify the adsorption sites of Xe in MFU-4*l* MOF. The results combined from TDS, quantum mechanical calculation, X-ray powder diffraction and MEM calculations indicate clearly that only one preferred adsorption site for Xe exists in MFU-4*l* which is located in the corner of the large pores of the bimodal pore structure. Furthermore, the small pores are not occupied by xenon at all. In contrast studies of hydrogen adsorption in MFU-4*l* showed that the smaller H2 molecules occupy both types of pores.[14]

## Acknowledgements

This work has been done in the framework of the European master program in Functional Advanced Materials Engineering (FAME). The partial support of the German Research Foundation (SPP-1662) is gratefully acknowledged.

## References

1 R. E. Morris and P. S. Wheatley, *Angew. Chem., Int. Ed.*, 2008, **47**, 4966–4981.
2 P. D. C. Dietzel, V. Besikiotis and R. Blom, *J. Mater. Chem.*, 2009, **19**, 7362–7370.

3 D. S. Sholl and S. Keskin, *Ind. Eng. Chem. Res.*, 2009, **48**, 914–922.
4 A. U. Czaja, N. Trukhan and U. Müller, *Chem. Soc. Rev.*, 2009, **38**, 1284–1293.
5 F. Xu, C. Z. Mu and W. Lei, *Prog. Chem.*, 2007, **19**, 1345–1356.
6 T. Duren, Y. S. Bae and R. Q. Snurr, *Chem. Soc. Rev.*, 2009, **38**, 1237–1247.
7 F. M. Mulder, T. J. Dingemans, H. G. Schimmel, A. J. Ramirez-Cuesta and G. J. Kearley, *Chem. Phys.*, 2008, **351**, 72–76.
8 G. Seifert, B. Assfour and S. Leoni, *J. Phys. Chem. C*, 2010, **114**, 13381–13384.
9 S. Kaskel, J. Getzschmann, I. Senkovska, D. Wallacher, M. Tovar, D. Fairen-Jimenez, T. Duren, J. M. van Baten and R. Krishna, *Microporous Mesoporous Mater.*, 2010, **136**, 50–58.
10 W. Zhou, H. Wu, J. M. Simmons, G. Srinivas and T. Yildirim, *J. Phys. Chem. Lett.*, 2010, **1**, 1946–1951.
11 J. H. Luo, H. W. Xu, Y. Liu, Y. S. Zhao, L. L. Daemen, C. Brown, T. V. Timofeeva, S. Q. Ma and H. C. Zhou, *J. Am. Chem. Soc.*, 2008, **130**, 9626–9627.
12 J. S. Chang, P. M. Forster, J. Eckert, B. D. Heiken, J. B. Parise, J. W. Yoon, S. H. Jhung and A. K. Cheetham, *J. Am. Chem. Soc.*, 2006, **128**, 16846–16850.
13 B. Panella, M. Hirscher and B. Ludescher, *Microporous Mesoporous Mater.*, 2007, **103**, 230–234.
14 D. Denysenko, M. Grzywa, M. Tonigold, B. Streppel, I. Krkljus, M. Hirscher, E. Mugnaioli, U. Kolb, J. Hanss and D. Volkmer, *Chem.–Eur. J.*, 2011, **17**, 1837–1848.
15 I. Krkljus and M. Hirscher, *Microporous Mesoporous Mater.*, 2011, **142**, 725–729.
16 Bruker AXS, TOPAS version 4.1, 2007.
17 F. Allen, *Acta Crystallogr., Sect. B: Struct. Sci.*, 2002, **58**, 380–388.
18 A. Le Bail, H. Duroy and J. L. Fourquet, *Mater. Res. Bull.*, 1988, **23**, 447–452.
19 R. W. Cheary, A. A. Coelho and J. P. Cline, *J. Res. Natil. Inst. Stand. Technol.*, 2004, **109**, 1–25.
20 S. Lambert and F. Guillet, *J. Appl. Crystallogr.*, 2008, **41**, 153–160.
21 A. Coelho, *J. Appl. Crystallogr.*, 2000, **33**, 899–908.
22 V. Favre-Nicolin and R. Cerny, *J. Appl. Crystallogr.*, 2002, **35**, 734–743.
23 R. Kitaura, S. Kitagawa, Y. Kubota, T. C. Kobayashi, K. Kindo, Y. Mita, A. Matsuo, M. Kobayashi, H. C. Chang, T. C. Ozawa, M. Suzuki, M. Sakata and M. Takata, *Science*, 2002, **298**, 2358–2361.
24 R. Matsuda, R. Kitaura, S. Kitagawa, Y. Kubota, R. V. Belosludov, T. C. Kobayashi, H. Sakamoto, T. Chiba, M. Takata, Y. Kawazoe and Y. Mita, *Nature*, 2005, **436**, 238–241.
25 S. van Smaalen, L. Palatinus and M. Schneider, *Acta Crystallogr., Sect. A: Fundam. Crystallogr.*, 2003, **59**, 459–469.
26 M. Sakata and M. Sato, *Acta Crystallogr., Sect. A: Fundam. Crystallogr.*, 1990, **46**, 263–270.
27 R. Dovesi, V. R. Saunders, C. Roetti, R. Orlando, C. M. Zicovich-Wilson, F. Pascale, B. Civalleri, K. Doll, N. M. Harrison, I. J. Bush, P. D'Arco and M. Llunell, CRYSTAL09, *CRYSTAL09 User's Manual*, University of Torino, Torino, 2009.
28 J. P. Perdew, K. Burke and M. Ernzerhof, *Phys. Rev. Lett.*, 1996, **77**, 3865–3868.
29 SCM, Scientific Computing & Modelling, Amsterdam, 2012.
30 S. Grimme, J. Antony, S. Ehrlich and H. Krieg, *J. Chem. Phys.*, 2010, **132**, 154104–154119.
31 P. Ryan, O. K. Farha, L. J. Broadbelt and R. Q. Snurr, *AIChE J.*, 2011, **57**, 1759–1766.